# Oxygen transport in proton exchange membrane fuel cells with metal foam flow fields

**Oxygen transport in proton exchange membrane fuel cells with metal foam flow fields**

**(accepted for publication by Journal of Power Sources)**

Mengshan Suo [a], Kai Sun [a,*], Rui Chen [b], Zhizhao Che [a], Zhen Zeng [a], Qifeng Li [a], Xingxiao Tao [a], Tianyou Wang [a,**]

[a] State Key Laboratory of Engines, Tianjin University, Tianjin, 300072, PR China

[b] Department of Aeronautical and Automotive Engineering, Loughborough University, Loughborough, LE11 3TU, United Kingdom

**HIGHLIGHTS**

- Oxygen transport in PEM ofuel cells is studied by using lattice Boltzmann method.
- Metal foam flow field has stronger oxygen transport than channel-rib flow field.
- Increasing metal foam pore density/compression ratio facilitates oxygen transport.
- Reducing porosity suppresses/enhances oxygen transport at low/high inlet velocity.

**Keywords:**

PEM fuel Cell; Metal foam flow field; Lattice Boltzmann method; Oxygen transport

**ABSTRACT**

Metal foam flow fields have shown great potential in improving the performance of proton xchange membrane (PEM) fuel cells, while their effect on the oxygen transport process remains inadequately understood. In this study, oxygen transport in metal foam flow fields (under zero-humidity operating conditions) is simulated by using a three-dimensional multi-species lattice Boltzmann model. Comparison is done between the metal foam flow field and the conventional channel-rib flow field, and parametric studies are conducted on the metal foam porosity, pore density, and compression ratio. Results show that the metal foam flow field enhances mass transfer of oxygen to the catalyst layer and improves the oxygen distribution homogeneity. Within the range of parameters considered, decrease in the metal foam porosity yields nonmonotonic variation of the mass transfer rate of oxygen to the catalyst layer, which increases at high inlet velocities (higher than 2 m/s) but decreases at low inlet velocities (less than 2 m/s). The increase in metal foam pore density and compression ratio leads to enhanced mass transfer of oxygen, which becomes increasingly prominent at high inlet velocity. The results of this study could be insightful for the implementation of metal foam flow fields in PEM fuel cells.

## 1. Introduction

Oxygen transport is a key issue to improve the performance of proton exchange membrane (PEM) fuel cells [1,2]. In a PEM fuel cell, the reactant gas is pumped into the flow field and then diffuses into the catalyst layer (CL) through the gas diffusion layer (GDL). After that, the oxygen reduction reaction occurs in the cathode CL, and the hydrogen oxidation reaction occurs in the anode CL. A poor reactant gas transport could lead to a low reactant concentration at the catalyst sites and cause a large concentration over-potential. Since oxygen transport is slower than hydrogen transport and the oxygen reduction reaction is much less efficient, design and optimization of the cathode flow field are more critical in PEM fuel cell development [3,4].

Conventional types of flow field such as parallel, serpentine, and parallel-serpentine usually have a limited mass transfer capability. On the one hand, conventional flow fields are generally machined on bi polar plates using the channel-rib structures, which may hinder gas transport and cause non-

uniform distribution of oxygen. On the other hand, since the dominant gas flow direction in the channel-rib flow field is parallel to the GDL surface, normal advection is rather weak and hence oxygen transport to the CL is predominantly by molecular diffusion.

Metal foams are highly porous materials (up to 98%) with three-dimensional (3D) pore structures. Due to the lightweight, the excellent electrical conductivity, and the high thermal conductivity, metal foams have received increasing attention for application in PEM fuel cells as flow fields [5–7]. In recent years, a number of experimental and computational works showed that the metal foam flow field can improve the reactant transport [8–11], water management [12–16], performance [17–22], and the cold start behavior [23,24] of PEM fuel cells. Specifically, Fly et al. [9] compared different flow fields using optical visualization and observed that the diffusion time for the reactant to cover 80% of the flow field area for the metal foam flow field was 61% faster than that without a flow field. Wu et al. [14] employed neutron imaging and observed that the metal foam flow field improved the uniformity of liquid water distribution and improved the tolerance to dehydration. Kumar and Reddy [17] compared the performance of PEM fuel cells with Ni-Cr foam flow field, stainless steel foam flow field, carbon cloth flow field, and conventional channel-rib flow field, among which the Ni-Cr foam flow field ranked the best. Jo and Ju [20] numerically investigated the performance and transport characteristics of PEM fuel cells with metal foam flow fields. The results showed that the metal foam flow field had less severe oxygen depletion, better membrane hydration, and more uniform current density, owing to the synergistic effects of weaker convective flow and absence of channel-rib structures. Azarafza et al. [22] numerically showed that the metal foam flow field increased by about 50% compared to the parallel flow field, possibly owing to the low liquid water saturation and the decreased transport resistance. Huo et al. [23] showed that the cold start performance of PEM fuel cells with metal foam flow field was improved compared to parallel flow field under galvanostatic control.

The structural parameters of metal foams such as porosity, pore size, pore density, and compression ratio significantly affect the fuel cell performance. Park et al. [25] experimentally found that the fuel cell performance was improved with the decrease of porosity when the porosity was higher than 50.1%. In contrast, Afshari et al. [26] numerically observed that the current density increased with the metal foam porosity within the range of 70%–85%. Shin et al. [27] found the pore size of 800 μm yielded the best performance. Park et al. [25] observed improved fuel cell performance with the decrease of the metal foam pore size and attributed it to the reduced charge transfer resistance and mass transfer resistance. Liu et al. [28] found that the fuel cell performance significantly increased with the metal foam compression ratio.

The abovementioned worthy advances identified significant influence of the metal foam flow field on the fuel cell performance, while the underlying physics still remains inadequately understood. In this work, we aim to numerically investigate the oxygen transport in metal foam flow fields (under zero-humidity operating conditions), with particular interest on the influence of structural parameters such as porosity, pore density, and compression ratio of the metal foam. In the following, numerical method, results and discussion, and conclusions will be sequentially presented in Section 2 to Section 4.

## 2. Numerical method

### 2.1. Multi-species single-phase lattice Boltzmann model

Lattice Boltzmann method (LBM) is a pore-scale numerical method that has been applied for simulating fluid flow and transport phenomena in the heterogeneous and anisotropic porous media

of PEM fuel cells [29,30]. Compared with conventional numerical methods, LBM is efficient in parallelization and complex-geometry wall treatment in porous media [31–33]. The lattice Boltzmann equation (LBE) for multi-species (oxygen, nitrogen, and water vapor) with a single relaxation time collision operator is:

$$f_{k,i}(x + e_i\Delta t, t + \Delta t) - f_{k,i}(x,t) = -\frac{1}{\tau_k}\left(f_{k,i}(x,t) - f_{k,i}^{eq}(x,t)\right) \quad (1)$$

where $f_{k,i}(x,t)$ is the density distribution function for the $k$ th species with the discrete velocity $e_i$ at position $x$ and time $t$, $\tau$ is the collision time that related to the kinematical viscosity $v = c_s^2(\tau - 0.5)$, and $f_{k,i}^{eq}$ is the equilibrium density distribution function in the form of:

$$f_{k,i}^{eq} = \rho_k w_i \left[1 + \frac{e_i \cdot u^{eq}}{c_s^2} + \frac{(e_i \cdot u^{eq})^2}{2c_s^4} + \frac{u^{eq} \cdot u^{eq}}{2c_s^2}\right] \quad (2)$$

where $w_i$ is the weight factor, $c_s$ is the lattice sound speed. For the D3Q19 lattice scheme (3 dimensions and 19 discrete velocities) adopted in this study, $w_0 = 1/3$, $w_{1-6} = 1/18$, $w_{7-18} = 1/36$, $c_s = c/\sqrt{3}$, where $c = \Delta x/\Delta t$ is the lattice speed with Δx being the lattice spacing and Δt being the time step.

The evolution of LBE consists of collision and streaming processes. After each cycle of "collision-streaming", the specie density $\rho_k$ and velocity $u_k$ can be calculated by:

$$\rho_k = \sum_i f_{k,i} \quad (3)$$

$$u_k = \frac{\sum_i f_{k,i} e_i}{\rho_k} \quad (4)$$

The composite velocity $u_k^{eq}$ is used to couple the LBEs for different species [34] by:

$$u_k^{eq} = \frac{\sum_k u_k \rho_k / \tau_k}{\sum_k \rho_k / \tau_k} \quad (5)$$

2.2. Electrochemical reaction boundary

The CL is simplified as a reactive surface due to its substantially smaller pore structures compared to the flow field and GDL. Referring to Molaeimanesh et al. [35–37] and Ashorynejad et al. [38–40], the modified half-way bounce-back boundary condition [41] is validated and used to model the cathode electrochemical reaction ($O_2 + 4H^+ + 4e^- \rightarrow 2H_2O$) of PEM fuel cells in this study. Specifically, the unknown density distribution functions for each species on the reactive surface can be calculated as follows. For nitrogen, half-way bounce-back boundary [42] is taken since no reaction occurs:

$$f_{N_2,i=3,8,9,17,18} = f_{N_2,i=6,11,12,14,15} \quad (6)$$

For oxygen/water vapor, modified half-way bounce-back boundary is employed to account for the oxygen consumption/water vapor pro duction in the electrochemical reaction:

$$f_{O_2,i=6,11,12,14,15} = (1 - k_{sr}^{LB}) f_{O_2,i=6,11,12,14,15} \quad (7)$$

$$f_{H_2O,i=3,8,9,17,18} = \frac{2M_{H_2O}}{M_{O_2}} k_{sr}^{LB} f_{O_2,i=6,11,12,14,15} \quad (8)$$

where $M$ is the molar mass, $k_{sr}^{LB}$ is the dimensionless surface reaction constant:

$$k_{sr}^{LB} = \left(\frac{6k_{st}\Delta t}{\Delta x}\right) / \left(1 + \frac{k_{st}\Delta x}{2D_{O_2}}\right) \quad (9)$$

where $k_{sr}$ is the macroscopic surface reaction constant, and $D_{O_2}$ is the oxygen diffusion coefficient. Although water condensation is not taken into account, the species equation of water vapor is still required as its partial pressure would affect the transport of oxygen.

The reaction rate per unit area $r$" can be calculated by a first-order approximation $r^{"} = k_{sr} C_{O_2}$ , where $C_{O_2}$ denotes the oxygen concentration. By using the Butler-Volmer equation [35,39,43], the macroscopic surface reaction constant for the cathode CL $k_{sr}$ can be derived as:

$$k_{sr} = \frac{a}{4F}\left(\frac{j_{ref}}{C_{O_2,ref}}\right)\left[exp\left(\frac{\alpha_f F\eta}{RT}\right) - exp\left(-\frac{\alpha_r F\eta}{RT}\right)\right] \quad (10)$$

where $j$ is the current density, $j_{ref}$ is the reference current density, $C_{O_2,ref}$ is the reference oxygen concentration, $\alpha_f$ is the forward reaction transfer coefficient, $\alpha_r$ is the reverse reaction transfer coefficient, $\eta$ is the activation over-potential, $T$ is the operating temperature, $R$ is the universal gas constant, $F$ is the Faraday constant, and $a$ is the surface roughness factor. The values of these parameters are listed in **Table 1**.

*Table 1 Physical parameters and operating conditions.*

| **Parameter** | **Value** |
|---|---|
| Operating temperature (K) | 333 |
| Operating pressure (atm) | 1.0 |
| Faraday constant (C mol$^{-1}$) | 96485 |
| Universal gas constant (J mol$^{-1}$ K$^{-1}$) | 8.314 |
| Water vapor dynamic viscosity (kg m$^{-1}$ s$^{-1}$) | $4.11 \times 10^{-3}$ (T/291.15)$^{1.5}$ (T+120)$^{-1}$ [39] |
| Oxygen dynamic viscosity (kg m$^{-1}$ s$^{-1}$) | $8.46 \times 10^{-3}$ (T/292.15)$^{1.5}$ (T+127)$^{-1}$ [39] |
| Nitrogen dynamic viscosity (kg m$^{-1}$ s$^{-1}$) | $7.33 \times 10^{-3}$ (T/300.55)$^{1.5}$ (T+111)$^{-1}$ [39] |
| Oxygen diffusivity (m$^2$ s$^{-1}$) | $2.20 \times 10^{-5}$ (T/293)$^{1.5}$ (1/P) [44] |
| Reference current density (A m$^{-2}$) | $1.3874 \times 10^{-2}$ [45] |
| Reference oxygen concentration (mol m$^{-3}$) | 10.875 [43] |
| Transfer coefficient for the forward reaction | 0.5 [35,36,44] |
| Transfer coefficient for the reverse reaction | 1 [35,36,44] |
| Surface roughness factor | 2000 [35,36] |
| Activation over-potential (V) | 0.4 [39] |

It is noted that, the choice of $\alpha_f = 0.5$ and $\alpha_r = 1.0$ in the present study is consistent with Molaeimanesh et al. [35–37] and Ashorynejad et al. [38–40], although symmetric charge transfer coefficients are used more often. In the present simulations, since the activation over-potential is positive, the value of $exp(-\alpha_r F\eta/RT)$ is approximately 6 orders of magnitude smaller compared to $exp(\alpha_f F\eta/RT)$. Therefore, the value of the reverse reaction transfer coefficient hardly affects the simulation results.

2.3. Details of numerical simulation

In the present study, the abovementioned 3D multi-species LBM model with electrochemical reactions is used to simulate the oxygen transport of PEM fuel cells. The main assumptions include: (1) All the gas species are considered as ideal gases; (2) Water vapor condensation and liquid transport are ignored; (3) The fuel cell is operating at an isothermal condition with uniform temperature distribution; (4) The electrochemical reaction is first-order, i.e. the local current density and local oxygen consumption rate is proportional to the oxygen concentration.

3D structure of the GDL, as shown in Fig. 1(a), is reconstructed by using the stochastic generation method [46–48]. In this study, we reconstruct a 150-µm-thick GDL structure with a fiber diameter of 10 µm and a porosity of 78%. The representative unit cell structure [49–51] is adopted to reconstruct the metal foam structures. In this study, the tetrakaidecahedron is selected as the representative unit cell. As shown in **Fig. 1**(b), the tetrakaidecahedron metal foam is similar to the real metal foams since both of them have web-like structures with pores, cells, and ligaments.

**Fig. 1**(c) and (d) show the computational domains of two typical cases of the channel-rib flow field and the metal foam flow field, respectively. Both computation domains comprise a flow field zone, a GDL zone, and a CL surface ($Z = 0$). The size of the computational domain is 3.5 (length, $X$, flow direction) × 0.5 (width, $Y$) × 0.65 (height, $Z$) mm$^3$, and the length and the height of the flow field zone are 2.5 mm and 0.5 mm, respectively. The two opposite sides in the $X$ direction of the computational domain are set as the inlet ($X = 0$) and the outlet ($X = 3.5$ mm), while the two opposite sides in the Y direction are set as symmetry planes ($Y = 0$ and $Y = 0.5$ mm).

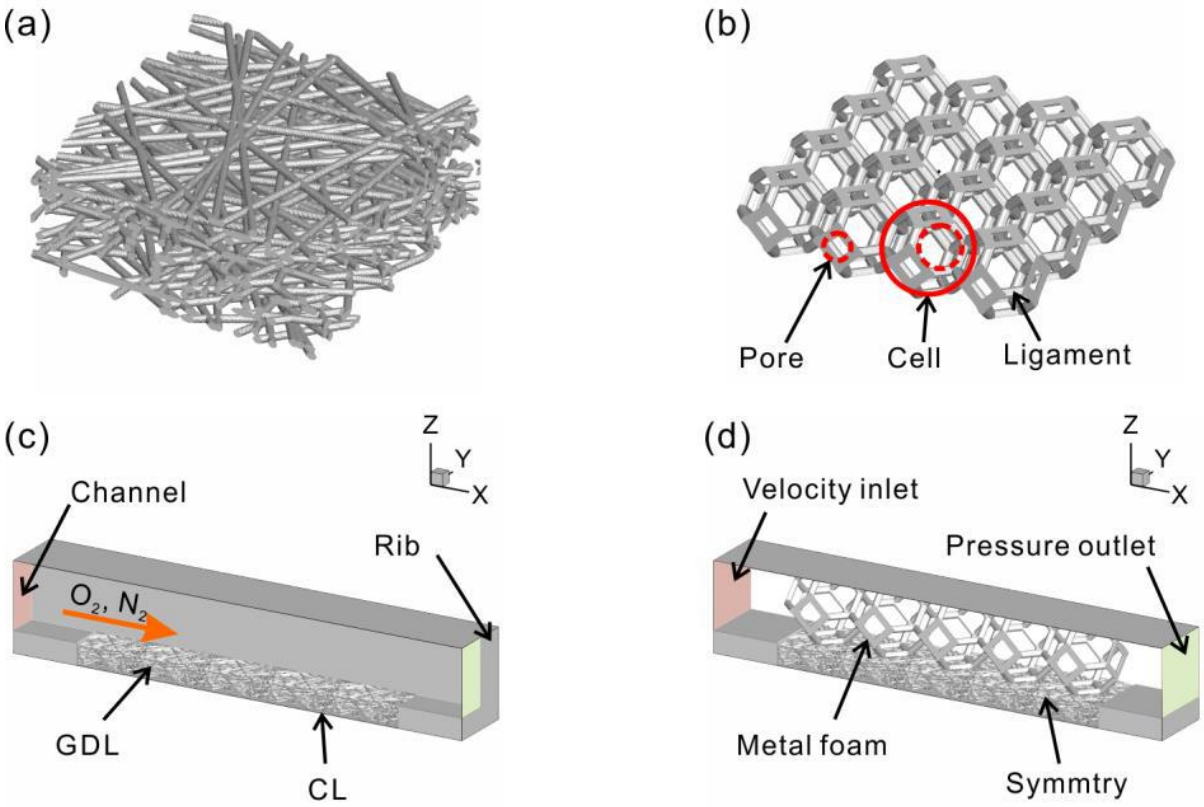


*Figure 1 (a) A typical GDL reconstructed based on the stochastic generation method; (b) Metal foam reconstructed by representative unit cell structure; (c) Computational domain for the case with the channel-rib flow field; (d) Computational domain for cases with metal foam flow field.*

The Zou-He method [52] is used to impose the velocity boundary condition and pressure boundary condition. The inlet velocity for the metal foam flow field ranges from 1 m/s to 5 m/s, approximately corresponding to the flow field length of 5 cm – 25 cm at a stoichiometric ratio of 3 and a current density of 2.0 A/cm$^2$ (flow field height of 1 mm). At the outlet, the partial pressures of each species are assumed equal to the preceding nodes since only the total pressure is known. Moreover, except for the reactive CL surface, all the solid surfaces are set as no-slip surfaces by applying the half-way bounce-back scheme [42]. More de tails of the structural parameters and the flow conditions are listed in **Table 2**.

*Table 2 Structural parameters and flow conditions.*

| **Parameter** | **Value** |
|---|---|
| Channel length, height, width (mm) | 2.5, 0.5, 0.5 |
| Rib width (mm) | 0.5 |
| Metal foam porosity | 70%, 75%, 80%, 85%, 90%, 95% |
| Metal foam pore density (pores per inch) | 100, 200, 300, 400 |
| Metal foam compression ratio | 1, 2, 3, 4, 5 |
| GDL thickness (μm) | 150 [53] |
| GDL porosity | 78% [53] |
| Channel inlet velocity (m $s^{-1}$) | 10 |
| Metal foam inlet velocity (m $s^{-1}$) | 1, 2, 3, 4, 5 |
| Oxygen mole fraction in the inlet air | 0.21 [35,36] |
| Nitrogen mole fraction in the inlet air | 0.79 [35,36] |
| Water vapor mole fraction in the inlet air | 0 [35,36] |

According to the grid-dependency test, a lattice spacing of 5 μm is adopted in the present study to balance between the computational accuracy and computational cost, with the total lattice number reaching 9.1 million. The LBM simulation is conducted in a parallel $C^{++}$ code developed in-house. Each case takes about 100 h by paralleling 28 Intel Skylake CPU cores (2.6 GHz). A more detailed validation of the numerical method can be found in the Supplementary Material.

## 3. Results and discussion

### 3.1. Comparison of the metal foam flow field and channel-rib flow field

Firstly, we compare the channel-rib flow field and the metal foam flow field on oxygen transport. The inlet mass flow rate is identical for two flow fields. The metal foam considered here has a porosity of 95% and a pore density of 100 ppi (pores per inch).

The velocity component in the stream-wise direction $U_X$ determines the gas retention time and affects the diffusion of oxygen. **Fig. 2**(a) shows the distribution of $U_X$ ($X = 2$ mm plane) of the channel-rib flow field and the metal foam flow field. Since the inlet area of the channel-rib flow field is partially blocked by the rib structure, the mean $U_X$ of the metal foam flow field (5.25 m/s) is substantially lower than that of the channel-rib flow field (10.08 m/s), indicating that the metal foam flow field has a longer gas retention time and therefore benefits oxygen diffusion to CL. The velocity component in the through-plane (TP) direction $U_Z$ measures the convective transport of oxygen towards CL. **Fig. 2**(b) and (c) compare the distribution of $U_Z$ ($X = 2$ mm plane) of the two flow fields. As highlighted by the circles in **Fig. 2**(b), the intricate ligaments of the metal foam disturb the gas flow and therefore yield increased $U_Z$ in both flow field and GDL. By further quantifying the intensity of TP convection using the volume-averaged convection velocity UC:

$$U_C = \frac{1}{V}\int |U_Z|\, dV \tag{11}$$

we find that UC in the metal foam flow field (0.531 m/s) is nearly one order of magnitude greater than that in the channel-rib flow field (0.0636 m/s), indicating the convective mass transfer could be substantially enhanced. In addition, the normalized transport area between the flow field and the GDL $A_{Trans}/A_{CL}$ (normalized by the area of CL) is also significantly higher for the metal foam (0.87) compared to the channel-rib (0.50), which also benefits oxygen transport to the CL.

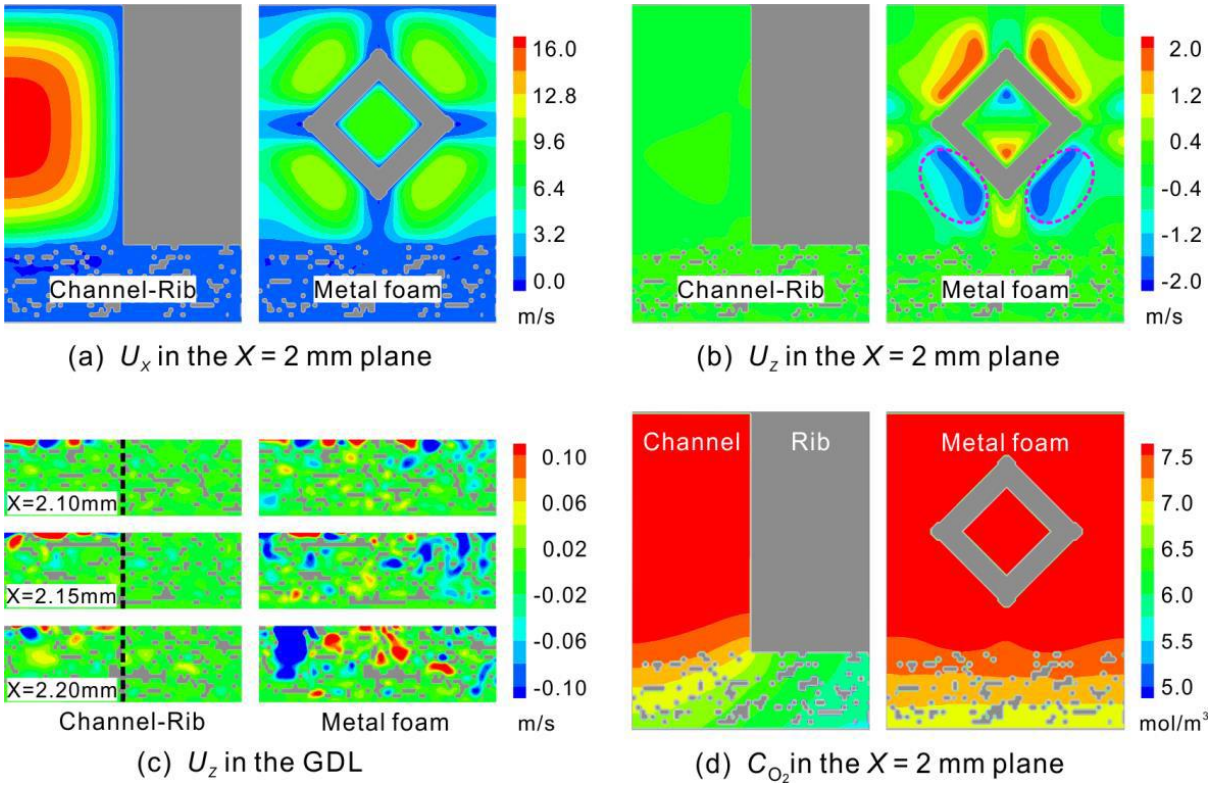


*Figure 2 (a) Comparison of UX in the X = 2 mm plane; (b) Comparison of UZ in the X = 2 mm plane; (c) Comparison of UZ in the GDL; (d) Comparison of CO2 in the GDL.*

**Fig. 2**(d) compares the distribution of oxygen concentration ($X = 2$ mm plane) of the channel-rib flow field and the metal foam flow field. For the channel-rib flow field, the oxygen concentration in the GDL reduces continuously from the under-channel region to the under-rib region, which may cause significant concentration loss at high current density conditions. For the metal foam flow field, in contrast, the oxygen concentration distribution appears to be much more uniform. The uniformity index of the CL oxygen concentration, $U_{O_2} = \int \frac{\left|C_{O_2}^{local} - C_{O_2}^{ave}\right|}{C_{O_2}^{ave}} dS/S$ , is computed as 0.0129 for the metal foam flow field and 0.0508 for the channel-rib flow field, indicating metal foam flow fields effectively improves the uniformity of oxygen distribution in the CL. As a result, the average current density for the metal foam flow field (1.86 A/cm$^2$) is improved compared to the channel-rib flow field (1.69 A/cm$^2$). Since the current density is proportional to the oxygen consumption rate and the oxygen consumption rate equals the oxygen flux in the GDL, the current density can quantify the mass transfer rate of oxygen to the CL. Thereby, metal foam flow fields can enhance oxygen transport compared to channel-rib flow fields. Under large operating current density, enhanced oxygen transport helps to reduce the concentration loss. Therefore, metal foam flow fields usually show better performance compared to conventional channel-rib flow fields, as experimentally reported in Refs. [18,54].

### 3.2. Effect of metal foam porosity

Having shown the potential of metal foam in enhancing mass transfer in PEM fuel cells, we proceed to discuss the structural parameters of metal foams. We are particularly interested on three parameters of porosity, pore density and compression ratio (see **Fig. S2** in the Supplementary Material). Among them, porosity and pore density are independent intrinsic structural parameters of the metal foam, while compression ratio measures the extent of the “compression action” in real

applications. A compressed metal foam with compression ratio>1 would yield an increased porosity and an increased pore density (TP direction) simultaneously.

We first consider the porosity, namely the ratio of the pore volume to the total volume of the porous media. In this section, the ligament diameter of metal foams is varied within 45 μm – 124 μm to achieve different metal foam porosities from 70% to 95% (see **Fig. S2**(a) in the Supplementary Material), which are common for metal foams in PEM fuel cell applications.

**Fig. 3** shows the distribution of $U_Z$ ($U_{inlet} = 5$ m/s) of the metal foam flow fields with porosities of 90%, 85%, and 80%. With the decrease of metal foam porosity, the diameter of ligaments (gray color) increases. For metal foams with lower porosity, thicker ligaments disturb more gas and increase the velocity component in the TP direction. Therefore, as shown in **Fig. 4**(a), the average convection velocity $U_C$ in the flow field increases with the decrease of metal foam porosity. The increased average convection velocity $U_C$ in the flow field further increases the average convection velocity $U_C$ in the GDL (see **Fig. 4**(b)), which is beneficial for convective transport. In addition, since $U_C$ is proportional to the inlet velocity, the improvement of $U_C$ with the decrease of metal foam porosity is more prominent at higher inlet velocity. On the other hand, the increased ligament diameter decreases the normalized trans port area between the metal foam flow field and the GDL. As shown in **Fig. 4**(c), the blue color denotes the contact area between the metal foam flow field and the GDL that cannot be utilized for gas transport. As the metal foam porosity decreases from 95% to 70%, the normalized transport area between the flow field and the GDL decreases from 0.87 to 0.62, which is not favored for oxygen diffusion.

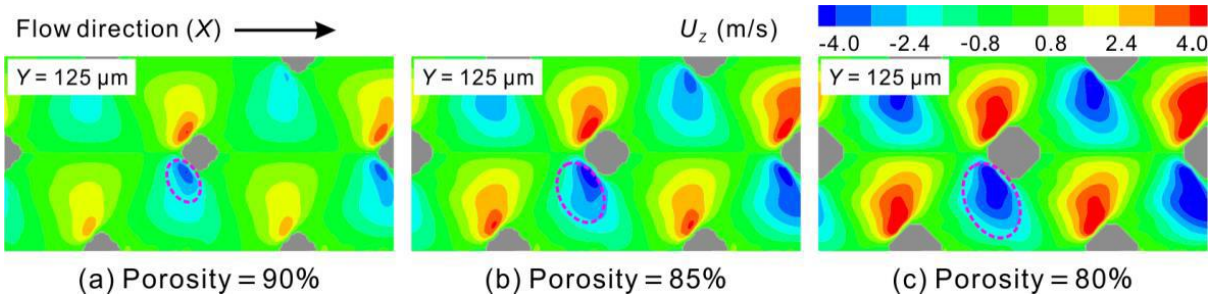


*Figure 3 Distribution of $U_Z$ for metal foam flow fields with different porosities ($U_{inlet} = 5$ m/s).*

The variation of current density with porosity is shown in **Fig. 4**(d), which exhibits distinct behavior at low and high inlet velocity. With the decrease of porosity, at low inlet velocity (e.g. 1 m/s), the weakened diffusional transport overwhelms the improved convective transport, leading to a reduced mass transfer rate of oxygen to the CL and hence a reduction of current density; At high inlet velocity (e.g. 3–5 m/s), however, the improvement in the convective transport is more prominent, yielding enhanced mass transfer and hence increased current density; At intermediate inlet velocity (e.g. 2 m/s), these two effects counteract, and the current density remains almost unchanged. Therefore, decrease in the metal foam porosity can improve the mass transfer rate of oxygen to the CL only when the inlet velocity is large enough.

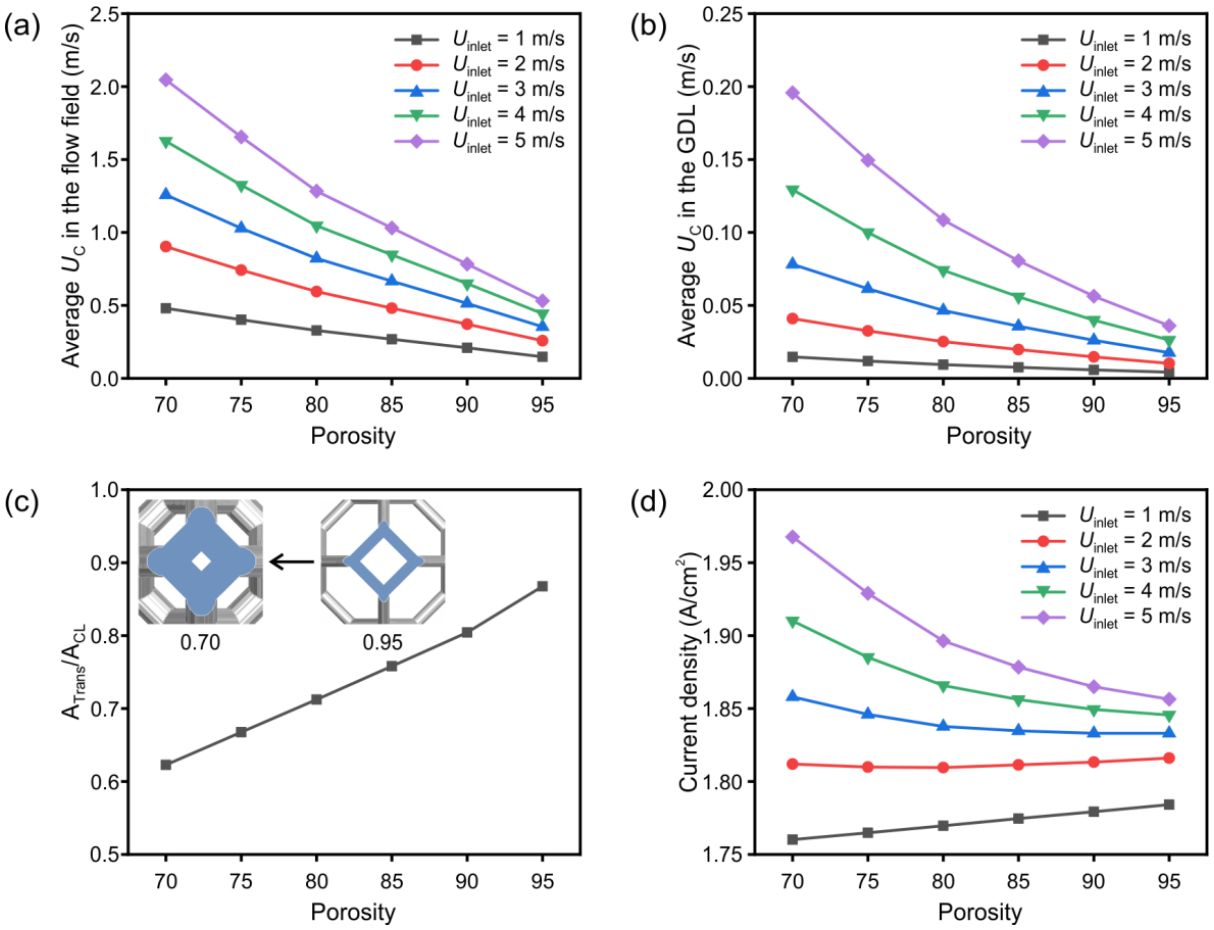


*Figure 4 Effect of metal foam porosity: (a) Average convection velocity in the flow field; (b) Average convection velocity in the GDL; (c) Normalized transport area between the metal foam flow field and the GDL; (d) Current density.*

Within the range of porosity considered in this paper, results suggest that metal foams with a higher porosity may be more suitable for PEM fuel cells with smaller-size flow fields (5–10 cm flow field length), which represent the most-widely used fuel cell unit in current experimental research and usually has an activation area of 25–50 cm$^2$ [55,56]. This is because diffusion dominants oxygen transport in smaller-size flow fields and a larger transport area between the metal foam flow field and the GDL is preferred. However, an optimal metal foam porosity was experimentally identified recently [25]. This can be explained by the trade-off between the electric conductivity and mass transfer rate, which de creases and increases with increasing metal foam porosity, respectively. On the contrary, metal foams with a lower porosity may be more suit able for PEM fuel cells with larger-size flow fields (15–25 cm flow field length), which represent the PEM fuel cell stacks utilized in automobile vehicles and usually have an activation area of 200–500 cm$^2$ [55–58]. Since reducing porosity enhances oxygen transport and electric conductivity simultaneously.

### 3.3. Effect of metal foam pore density

The pore density, usually quantified by ppi, is another key parameter of the metal foam flow field. At a fixed porosity, ppi decreases with increasing the average pore size. In this section, the porosity of the metal foams is fixed at 95%, and a number of cell sizes are considered, cor responding to the pore density of 100 ppi, 200 ppi, 300 ppi, and 400 ppi (see **Fig. S2**(b) in the Supplementary Material).

**Fig. 5** shows the distribution of $U_Z$ ($U_{inlet} = 5$ m/s) of the metal foam flow fields with different pore densities. At a fixed porosity, the number of ligaments (gray color) increases, and the diameter of ligaments (gray color) decreases with the increase of metal foam pore density. For metal foams with

a higher pore density, the increased number of ligaments induces more vortices and increases the velocity component in the TP direction. As shown in **Fig. 6**(a), the average convection velocity $U_C$ in the flow field increases with increasing metal foam pore density. At 5 m/s inlet velocity condition, $U_C$ in the flow field of 400-ppi metal foam (0.866 m/s) increases by 63% compared to that of the 100-ppi metal foam (0.531 m/s). Due to the smaller cell size of the high pore density metal foams, the convection regions are closer to the GDL, which enhances UC in the GDL. As shown in **Fig. 6**(b), UC in the GDL increases more prominently compared to the flow field. At 5 m/s inlet velocity condition, UC in the GDL of the 400-ppi metal foam (0.246 m/s) substantially increases about 583% compared with that of the 100-ppi metal foam (0.036 m/s). Therefore, the convective transport of oxygen increases significantly with the metal foam pore density. As shown in **Fig. 6**(c), with the increased ligament number and reduced ligament diameter, the normalized transport area between the metal foam flow field and the GDL remains insignificantly changed with the metal foam pore density, indicating that the diffusive transport of oxygen is less affected by the pore density.

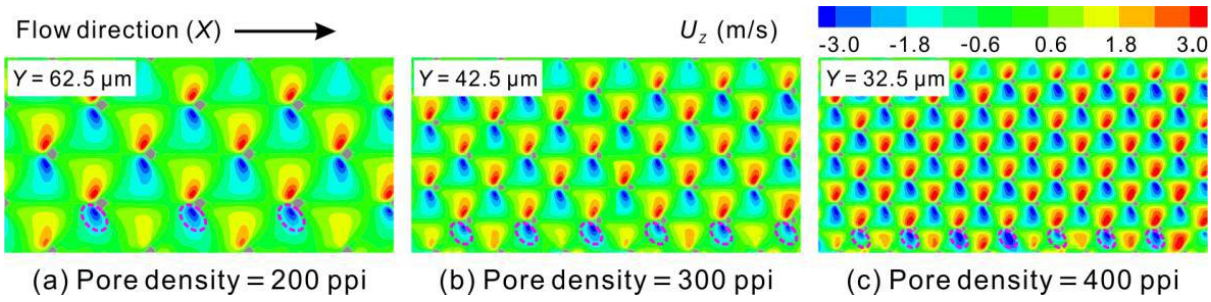


*Figure 5 Distribution of $U_Z$ for metal foam flow fields with different pore densities ($U_{inlet} = 5$ m/s).*

**Fig. 6**(d) shows the variation of current density with the metal foam pore density. Since the diffusive transport of oxygen barely changes with the metal foam pore density, the mass transfer rate of oxygen to the CL is mainly determined by convection. Therefore, the variation of the current density is consistent with the average convection velocity UC in the GDL, which increases with increasing metal foam pore density for all the inlet velocities. This suggests that metal foams with a higher pore density could be more suitable for PEM fuel cells regardless of the size of the flow field since the convective transport of oxygen is enhanced while the diffusive transport is not largely affected. Park et al. [25] experimentally found that the fuel cell performance improved with the metal foam pore density. They attributed such improvement to the constant ohmic resistance and the increased internal pressure. According to the present simulation results, the improvement can also be attributed to the enhanced oxygen transport that reduces the concentration loss.

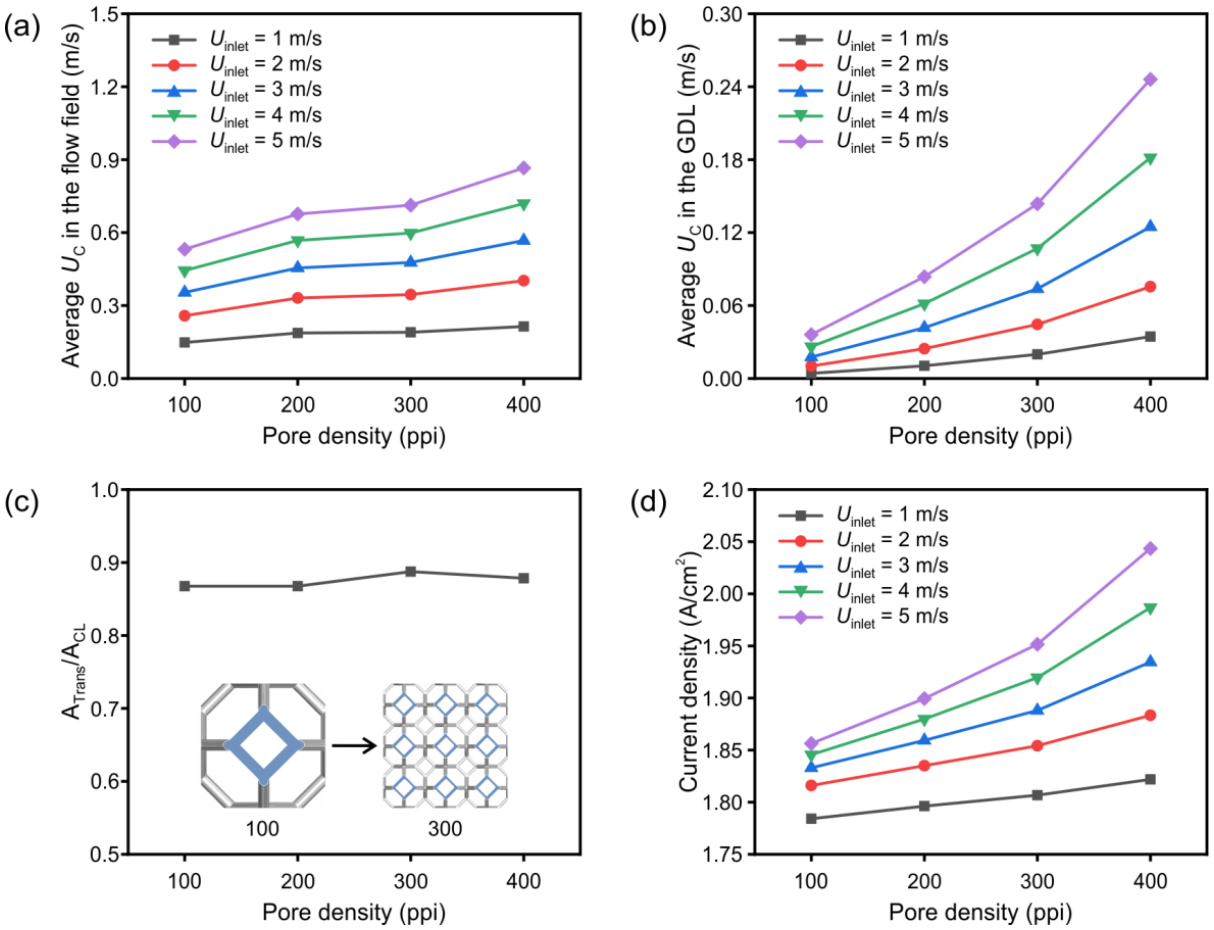


*Figure 6 Effect of metal foam pore density: (a) Average convection velocity in the flow field; (b) Average convection velocity in the GDL; (c) Normalized transport area between the metal foam flow field and the GDL; (d) Current density.*

### 3.4. Effect of metal foam compression ratio

Since commercial metal foams are always processed into several specific thicknesses, they are often compressed in fuel cells to achieve an appropriate height of the flow field while enhancing mechanical strength, electrical conductivity, and contact conductivity. Compression ratio is defined as the ratio of the pre-compression thickness to the post compression thickness of the metal foam sample. In this section, several cell heights (500 µm, 250 µm, 167 µm, 125 µm, and 100 µm) are considered, corresponding to compression ratios of 1 (uncompressed), 2, 3, 4, and 5 that cover a common range in PEM fuel cell studies (see **Fig. S2**(c) in the Supplementary Material). For all the metal foams considered in this section, pre-compression porosity and pore density are fixed at 95% and 100 ppi, respectively.

**Fig. 7** compares the distribution of $U_{CZ}$ ($U_{inlet} = 5$ m/s) of the metal foam flow fields with different compression ratios. The number of ligaments (gray color) increases while the diameter of ligaments (gray color) remains unchanged with increasing compression ratio. For metal foams with a higher compression ratio, the rise in ligament number disturbs more gas and increases the velocity component in the TP direction. As shown in Fig. 8(a), the average convection velocity $U_C$ in the flow field increases with increasing compression ratio. However, the improvement of $U_C$ in the flow field is slight when the compression ratio exceeds 2. For 5 m/s inlet velocity, $U_C$ in the metal foam flow field with a compression ratio of 5 (1.159 m/s) increases only about 25% compared with that of 2 (0.924 m/s). This is because that the reduced inter-ligament spacing in the TP direction tends to suppresses the further increase of UZ. Since the smaller cell height of the high compression ratio

metal foams, the convection regions are closer to the GDL. As shown in **Fig. 8**(b), UC in the GDL increases more prominently compared to the flow field. For 5 m/s inlet velocity, UC in the GDL with a compression ratio of 5 (0.292 m/s) increases over three times compared to that with a compression ratio of 2 (0.064 m/s). Therefore, the convective transport of oxygen tends to increase with the metal foam compression ratio. On the other hand, due to the smaller GDL-ligaments spacing, the increased compression ratio also yields a decreased transport area. As shown in **Fig. 8**(c), as the compression ratio increases from 1 to 5, the normalized transport area between the flow field and the GDL decreases from 0.87 to 0.82, indicating only a slight reduction in the diffusive transport of oxygen.

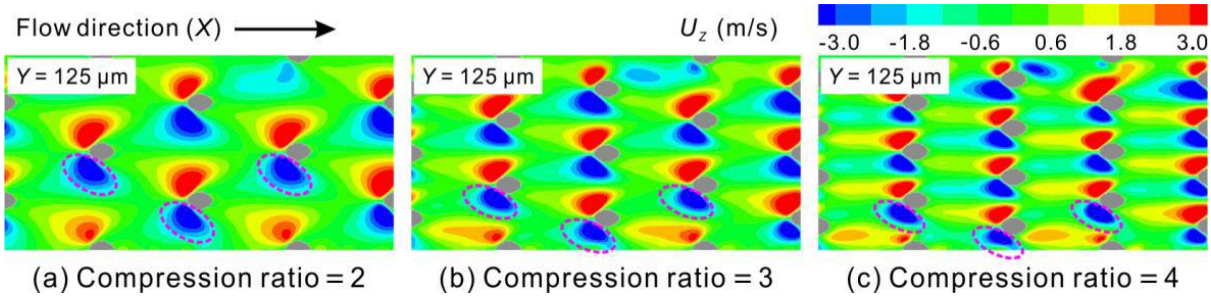


*Figure 7 Distribution of $U_Z$ for metal foam flow fields with different compression ratios ($U_{inlet} = 5$ m/s).*

**Fig. 8**(d) shows the variation of current density with the metal foam compression ratio under different inlet velocities. Since the diffusive transport of oxygen only slightly decreases with increasing metal foam compression ratio, the mass transfer rate of oxygen to the CL is mainly determined by convection. The variation of the current density with the metal foam compression ratio is consistent with the average convection velocity $U_C$ in the GDL, which increases with increasing metal foam compression ratio for all the inlet velocity conditions. Therefore, due to the reduced concentration loss, it can be observed that metal foam flow fields with higher compression ratios usually show better fuel cell performance in recent experiments [18,28].

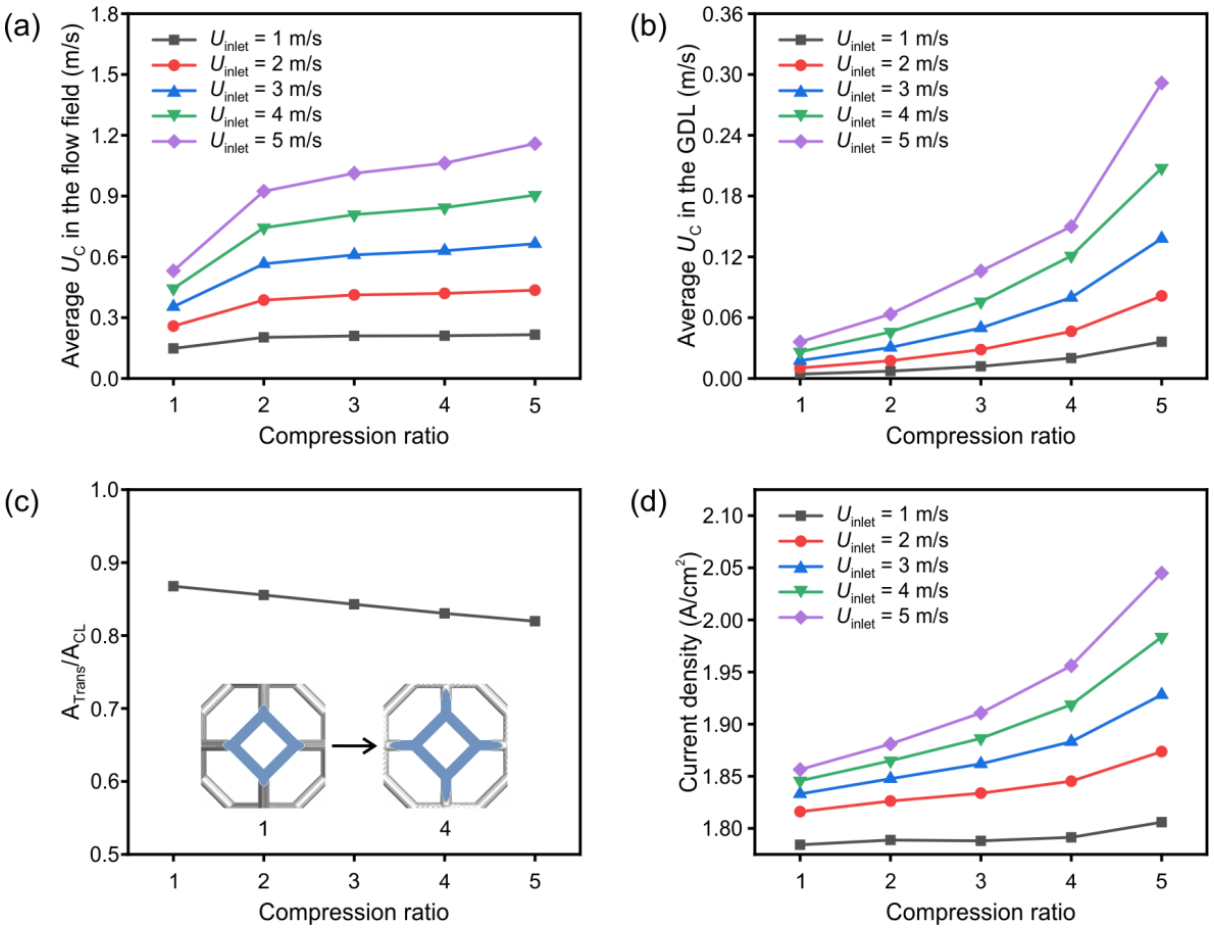


*Figure 8 Effect of metal foam compression ratio: (a) Average convection velocity in the flow field; (b) Average convection velocity in the GDL; (c) Normalized transport area between the metal foam flow field and the GDL; (d) Current density.*

Finally, it should be noted that in the present study, oxygen transport in PEM fuel cells is simulated by ignoring liquid water condensation and transport, which is not entirely realistic. The presence of liquid water may locally alter the pathway of oxygen transport, thereby affecting the statistical average behavior. Possibly, liquid water may suppress oxygen transport in GDL by increasing flow resistance, whereas promote oxygen transport in metal foam flow fields by enhancing convection. Moreover, the present results indicate that the improvement of oxygen transport is mainly ascribed to the enhancement of convection, which may also contribute to the discharge of liquid water. Further studies on oxygen transport with water condensation and transport is still merited.

## 4. Conclusions

In this paper, the effect of the metal foam flow field on the oxygen transport in PEM fuel cells under zero-humidity operating conditions is numerically investigated by using a 3D multi-species LBM model. To focus on the influence of structural parameters including porosity, pore density, and compression ratio, water vapor condensation and liquid transport are neglected in the simulations. Within the range of parameters considered in this paper, main conclusions are drawn as follows: (1) Compared to channel-rib flow fields, metal foam flow fields have prolonged gas retention time, intensified convective flow, and enlarged transport area between the flow field and the GDL, therefore are capable of increasing the mass transfer rate of oxygen to the CL and improve the oxygen distribution; (2) Thick ligaments in metal foams with low porosities facilitate the convection while suppress the diffusion. The decrease in metal foam porosity yields increased mass transfer rate of oxygen to the CL for high inlet velocities (higher than about 2 m/s) and decreased mass

transfer rate of oxygen to the CL for low inlet velocities (less than about 2 m/s); (3) The small cell size and thin ligaments in the high pore density metal foams facilitate the convection without much side effect on the diffusion. The increase in metal foam pore density therefore results in enhanced mass transfer rate of oxygen to the CL, and the enhancement tends to be increasingly prominent at high inlet velocities; (4) Similarly, the reduced cell height in compressed metal foams enhances convection and suppresses the diffusion only slightly, which yields enhanced mass transfer rate of oxygen to the CL and improves the current density. The results of this study could be insightful for the implementation of metal foam flow field in PEM fuel cells.

**CRediT authorship contribution statement**

Mengshan Suo: Methodology, Software, Validation, Formal analysis, Investigation, Data curation, Visualization, Writing – original draft. Kai Sun: Methodology, Formal analysis, Writing – review & editing. Rui Chen: Writing – review & editing. Zhizhao Che: Writing – review & editing. Zhen Zeng: Methodology. Qifeng Li: Formal analysis. Xing xiao Tao: Formal analysis. Tianyou Wang: Supervision, Conceptualization, Funding acquisition.

**Declaration of competing interest**

The authors declare that they have no known competing financial interests or personal relationships that could have appeared to influence the work reported in this paper.

**Acknowledgements**

The authors gratefully acknowledge the financial support from National Natural Science Foundation of China (No. 51920105010 and No. 51921004).

**Appendix A.** Supplementary data

Supplementary data to this article can be found online at https://doi.org/10.1016/j.jpowsour.2021.230937.

**References**

[1] H.-C. Liu, W.-M. Yan, C.-Y. Soong, F. Chen, H.-S. Chu, Reactant gas transport and cell performance of proton exchange membrane fuel cells with tapered flow field design, J. Power Sources 158 (2006) 78–87.

[2] F. Tiss, R. Chouikh, A. Guizani, A numerical investigation of reactant transport in a PEM fuel cell with partially blocked gas channels, Energy Convers. Manag. 80 (2014) 32–38.

[3] C.-Y. Soong, W.-M. Yan, C. Tseng, H.-C. Liu, F. Chen, H.-S. Chu, Analysis of reactant gas transport in a PEM fuel cell with partially blocked fuel flow channels, J. Power Sources 143 (2005) 36–47.

[4] Y. Yin, S. Wu, Y. Qin, O.N. Otoo, J. Zhang, Quantitative analysis of trapezoid baffle block sloping angles on oxygen transport and performance of proton exchange membrane fuel cell, Appl. Energy 271 (2020), 115257.

[5] W. Yuan, Y. Tang, X. Yang, Z. Wan, Porous metal materials for polymer electrolyte membrane fuel cells–A review, Appl. Energy 94 (2012) 309–329.

[6] W.C. Tan, L.H. Saw, H. San Thiam, J. Xuan, Z. Cai, M.C. Yew, Overview of porous media/metal foam application in fuel cells and solar power systems, Renew. Sustain. Energy Rev. 96 (2018) 181–197.

[7] Y. Zhang, Y. Tao, J. Shao, Application of porous materials for the flow field in polymer electrolyte membrane fuel cells, J. Power Sources 492 (2021), 229664.

[8] J. Carton, A.-G. Olabi, Three-dimensional proton exchange membrane fuel cell model: Comparison of double channel and open pore cellular foam flow plates, Energy 136 (2017) 185–195.

[9] A. Fly, D. Butcher, Q. Meyer, M. Whiteley, A. Spencer, C. Kim, P. Shearing, D. J. Brett, R. Chen, Characterisation of the diffusion properties of metal foam hybrid flow-fields for fuel cells using optical flow visualisation and X-ray computed tomography, J. Power Sources 395 (2018) 171–178.

[10] J.E. Park, J. Lim, S. Kim, I. Choi, C.-Y. Ahn, W. Hwang, M.S. Lim, Y.-H. Cho, Y.-E. Sung, Enhancement of mass transport in fuel cells using three-dimensional graphene foam as flow field, Electrochim. Acta 265 (2018) 488–496.

[11] G. Zhang, Z. Bao, B. Xie, Y. Wang, K. Jiao, Three-dimensional multi-phase simulation of PEM fuel cell considering the full morphology of metal foam flow field, Int. J. Hydrogen Energy 46 (2021) 2978–2989.

[12] J. Chen, Experimental study on the two phase flow behavior in PEM fuel cell parallel channels with porous media inserts, J. Power Sources 195 (2010) 1122–1129.

[13] A. Jo, S. Ahn, K. Oh, W. Kim, H. Ju, Effects of metal foam properties on flow and water distribution in polymer electrolyte fuel cells (PEFCs), Int. J. Hydrogen Energy 43 (2018) 14034–14046.

[14] Y. Wu, J. Cho, M. Whiteley, L. Rasha, T. Neville, R. Ziesche, R. Xu, R. Owen, N. Kulkarni, J. Hack, Characterization of water management in metal foam flow field based polymer electrolyte fuel cells using in-operando neutron radiography, Int. J. Hydrogen Energy 45 (2020) 2195–2205.

[15] Z. Bao, Y. Wang, K. Jiao, Liquid droplet detachment and dispersion in metal foam flow field of polymer electrolyte membrane fuel cell, J. Power Sources 480 (2020), 229150.

[16] Y. Wu, X. Lu, J. Cho, L. Rasha, M. Whiteley, T. Neville, R. Ziesche, N. Kardjilov, H. Markotter, ¨ I. Manke, Multi-length scale characterization of compression on metal foam flow-field based fuel cells using X-ray computed tomography and neutron radiography, Energy Convers. Manag. 230 (2021), 113785.

[17] A. Kumar, R.G. Reddy, Materials and design development for bipolar/end plates in fuel cells, J. Power Sources 129 (2004) 62–67.

[18] C.-J. Tseng, B.T. Tsai, Z.-S. Liu, T.-C. Cheng, W.-C. Chang, S.-K. Lo, A PEM fuel cell with metal foam as flow distributor, Energy Convers. Manag. 62 (2012) 14–21.

[19] Z. Wan, Y. Sun, C. Yang, X. Kong, H. Yan, X. Chen, T. Huang, X. Wang, Experimental performance investigation on the arrangement of metal foam as flow distributors in proton exchange membrane fuel cell, Energy Convers. Manag. 231 (2021), 113846.

[20] A. Jo, H. Ju, Numerical study on applicability of metal foam as flow distributor in polymer electrolyte fuel cells (PEFCs), Int. J. Hydrogen Energy 43 (2018) 14012–14026.

[21] A. Kumar, R.G. Reddy, Modeling of polymer electrolyte membrane fuel cell with metal foam in the flow-field of the bipolar/end plates, J. Power Sources 114 (2003) 54–62.

[22] A. Azarafza, M.S. Ismail, M. Rezakazemi, M. Pourkashanian, Comparative study of conventional and unconventional designs of cathode flow fields in PEM fuel cell, Renew. Sustain. Energy Rev. 116 (2019), 109420.

[23] S. Huo, N.J. Cooper, T.L. Smith, J.W. Park, K. Jiao, Experimental investigation on PEM fuel cell cold start behavior containing porous metal foam as cathode flow distributor, Appl. Energy 203 (2017) 101–114.

[24] S. Huo, L. Li, W. Shi, R. Wang, B. Lu, Y. Yin, C. Zhu, Y. Wang, K. Jiao, Z. Hou, Characteristics of cold start behavior of PEM fuel cell with metal foam as cathode flow field under subfreezing temperature, Int. J. Green Energy 18 (2021) 1129–1146.

[25] J.E. Park, W. Hwang, M.S. Lim, S. Kim, C.-Y. Ahn, O.-H. Kim, J.-G. Shim, D.W. Lee,

J.H. Lee, Y.-H. Cho, Achieving breakthrough performance caused by optimized metal foam flow field in fuel cells, Int. J. Hydrogen Energy 44 (2019) 22074–22084.

[26] E. Afshari, M. Mosharaf-Dehkordi, H. Rajabian, An investigation of the PEM fuel cells performance with partially restricted cathode flow channels and metal foam as a flow distributor, Energy 118 (2017) 705–715.

[27] D.K. Shin, J.H. Yoo, D.G. Kang, M.S. Kim, Effect of cell size in metal foam inserted to the air channel of polymer electrolyte membrane fuel cell for high performance, Renew. Energy 115 (2018) 663–675.

[28] R. Liu, W. Zhou, S. Li, F. Li, W. Ling, Performance improvement of proton exchange membrane fuel cells with compressed nickel foam as flow field structure, Int. J. Hydrogen Energy 45 (2020) 17833–17843.

[29] K.N. Kim, J.H. Kang, S.G. Lee, J.H. Nam, C.-J. Kim, Lattice Boltzmann simulation of liquid water transport in microporous and gas diffusion layers of polymer electrolyte membrane fuel cells, J. Power Sources 278 (2015) 703–717.

[30] F. Jinuntuya, M. Whiteley, R. Chen, A. Fly, The effects of gas diffusion layers structure on water transportation using X-ray computed tomography based Lattice Boltzmann method, J. Power Sources 378 (2018) 53–65.

[31] L. Chen, Q. Kang, Y. Mu, Y.-L. He, W.-Q. Tao, A critical review of the pseudopotential multiphase lattice Boltzmann model: methods and applications, Int. J. Heat Mass Tran. 76 (2014) 210–236.

[32] G. Molaeimanesh, H.S. Googarchin, A.Q. Moqaddam, Lattice Boltzmann simulation of proton exchange membrane fuel cells–A review on opportunities and challenges, Int. J. Hydrogen Energy 41 (2016) 22221–22245.

[33] A. Xu, W. Shyy, T. Zhao, Lattice Boltzmann modeling of transport phenomena in fuel cells and flow batteries, Acta Mech. Sin. 33 (2017) 555–574.

[34] X. Shan, H. Chen, Lattice Boltzmann model for simulating flows with multiple phases and components, Phys. Rev. 47 (1993) 1815–1819.

[35] G. Molaeimanesh, M. Akbari, A three-dimensional pore-scale model of the cathode electrode in polymer-electrolyte membrane fuel cell by lattice Boltzmann method, J. Power Sources 258 (2014) 89–97.

[36] G. Molaeimanesh, M. Nazemian, Investigation of GDL compression effects on the performance of a PEM fuel cell cathode by lattice Boltzmann method, J. Power Sources 359 (2017) 494–506.

[37] M. Nazemian, G. Molaeimanesh, Impact of carbon paper structural parameters on the performance of a polymer electrolyte fuel cell cathode via lattice Boltzmann method, Acta Mech. Sin. 36 (2020) 367–380.

[38] H.R. Ashorynejad, K. Javaherdeh, Investigation of a waveform cathode channel on the performance of a PEM fuel cell by means of a pore-scale multi-component lattice Boltzmann method, J. Taiwan Inst. Chem. Eng. 66 (2016) 126–136.

[39] H.R. Ashorynejad, K. Javaherdeh, H.E. Van den Akker, The effect of pulsating pressure on the performance of a PEM fuel cell with a wavy cathode surface, Int. J. Hydrogen Energy 41 (2016) 14239–14251.

[40] H.R. Ashorynejad, K. Javaherdeh, Evaluation of passive and active lattice Boltzmann method for PEM fuel cell modeling, Phys. Stat. Mech. Appl. 535 (2019), 121943.

[41] M. Kamali, S. Sundaresan, H. Van den Akker, J. Gillissen, A multi-component two-phase lattice Boltzmann method applied to a 1-D Fischer–Tropsch reactor, Chem. Eng. J. 207 (2012) 587–595.

[42] M.C. Sukop, D.T. Thorne, Lattice Boltzmann Modeling: an Introduction for Geoscientists and Engineers, first ed., Springer, Heidelberg, 2006.

[43] M.M. Mench, Fuel Cell Engines, first ed., John Wiley & Sons, New Jersey, 2008.

[44] T. Berning, D. Lu, N. Djilali, Three-dimensional computational analysis of transport phenomena in a PEM fuel cell, J. Power Sources 106 (2002) 284–294.

[45] A. Parthasarathy, S. Srinivasan, A.J. Appleby, C.R. Martin, Temperature dependence of the electrode kinetics of oxygen reduction at the platinum/Nafion® interface—a microelectrode investigation, J. Electrochem. Soc. 139 (1992) 2530.

[46] K. Schladitz, S. Peters, D. Reinel-Bitzer, A. Wiegmann, J. Ohser, Design of acoustic trim based on geometric modeling and flow simulation for non-woven, Comput. Mater. Sci. 38 (2006) 56–66.

[47] L. Hao, P. Cheng, Lattice Boltzmann simulations of water transport in gas diffusion layer of a polymer electrolyte membrane fuel cell, J. Power Sources 195 (2010) 3870–3881.

[48] M. Shojaeefard, G. Molaeimanesh, M. Nazemian, M. Moqaddari, A review on microstructure reconstruction of PEM fuel cells porous electrodes for pore scale simulation, Int. J. Hydrogen Energy 41 (2016) 20276–20293.

[49] Y. Kwon, R. Cooke, C. Park, Representative unit-cell models for open-cell metal foams with or without elastic filler, Mater. Sci. Eng., A 343 (2003) 63–70.

[50] A. Festuccia, D. Chiappini, G. Bella, Open-cell metal foam mesh generation for lattice Boltzmann simulations, J. Porous Media 21 (2018) 423–439.

[51] A. Fly, K. Kim, J. Gordon, D. Butcher, R. Chen, Liquid water transport in porous metal foam flow-field fuel cells: a two-phase numerical modelling and ex-situ experimental study, Energies 12 (2019) 1186.

[52] Q. Zou, X. He, On pressure and velocity boundary conditions for the lattice Boltzmann BGK model, Phys. Fluids 9 (1997) 1591–1598.

[53] Q. Chen, Z. Niu, H. Li, K. Jiao, Y. Wang, Recent progress of gas diffusion layer in proton exchange membrane fuel cell: two-phase flow and material properties, Int. J. Hydrogen Energy 46 (2021) 8640–8671.

[54] M. Kim, C. Kim, Y. Sohn, Application of metal foam as a flow field for PEM fuel cell stack, Fuel Cell. 18 (2018) 123–128.

[55] J. Cho, H.-S. Kim, K. Min, Transient response of a unit proton-exchange membrane fuel cell under various operating conditions, J. Power Sources 185 (2008) 118–128.

[56] S. Shimpalee, S. Greenway, D. Spuckler, J. Van Zee, Predicting water and current distributions in a commercial-size PEMFC, J. Power Sources 135 (2004) 79–87.

[57] Y. Wang, C.-Y. Wang, Ultra large-scale simulation of polymer electrolyte fuel cells, J. Power Sources 153 (2006) 130–135.

[58] S. Shimpalee, S. Hirano, M. DeBolt, V. Lilavivat, J. Weidner, Y. Khunatorn, Macro scale analysis of large scale PEM fuel cell flow-fields for automotive applications, J. Electrochem. Soc. 164 (2017), E3073.